Carbon 231 (2025) 119711

Contents lists available at ScienceDirect

Carbon

journal homepage: www.elsevier.com/locate/carbon

The effects of crystal orientation and common coal impurities on electronic conductivity in copper–carbon composites

K. Nepal [a,*], C. Ugwumadu [a], F. Kraft [b], Y. Al-Majali [c], D.A. Drabold [a]

[a] Department of Physics and Astronomy, Nanoscale and Quantum Phenomena Institute (NQPI), Ohio University, Athens, 45701, OH, USA
[b] MetalKraft Technologies LLC, 38810 OH 689, Albany, 45710, OH, USA
[c] Institute for Sustainable Energy and the Environment (ISEE), Ohio University, Athens, 45701, OH, USA

ARTICLE INFO

Keywords:
Graphene
Composites
Coal
Electronic conductivity
Registry

ABSTRACT

The electronic conduction properties of copper–graphene composite materials including common coal impurities are studied. Exploring the transport properties for three crystallographic orientations [(111), (110), and (100)] of copper in copper–graphene composites, a strong orientational dependence on electronic conductivity is shown. Graphene exhibits near-ideal registries for (111) and (110) orientations, forming a connected network between grains that enables efficient carrier transport. The influence of non-carbon elements: nitrogen (N), oxygen (O), and sulfur (S) in graphene, representing possible structures in coal-based graphene are investigated. N, O, and S in graphene negatively impact the composite's electronic conductivity relative to pristine graphene. A new method is introduced for visualizing the spatial distribution of electrical conduction activity in materials using the square of the electronic charge density near the Fermi level, based on the work of Mott. We call this technique the N^2 method.

1. Introduction

Enhancing the electronic conductivity of face-centered cubic (FCC) metals, such as copper, is a significant area of research in material physics and engineering. Any performance improvements are valuable given copper's critical role in power transmission and distribution, motors, and generators. Traditional alloying methods using additives like silver, niobium, and silicon carbide [1–3] can enhance copper's mechanical properties but often compromise its electronic conductivity. However, recent advancements in incorporating graphene additives into copper matrices have shown promise in developing copper–graphene composites with improved electronic conductivity [4–10].

Among the alloying methods used to balance mechanical performance and electronic conductivity, the solid-phase extrusion method for metal–graphene composite wires has proven significant in processing samples with enhanced electronic conductivity [11–13]. During solid-phase processing, which involves thermophysical treatments such as high-temperature annealing, friction heating, and shear stress, materials can develop complex microstructures. In this context, it is crucial to determine whether interface alignments and the improved density of states at the Fermi level are universally relevant across metal-grain composites for achieving enhanced conductivity on a broader scale. The primary limitation in electronic conduction in metals is grain boundaries. This work provides additional evidence that these boundaries are "dressed" by graphene-type material, which significantly impacts the overall conductivity.

The ongoing graphite deficit [14] poses a significant challenge to the growth of the metal–graphene composites industry. In response, there has been a shift towards integrating coal-derived graphene [15–19], which offers a cost-effective and scalable approach to metal–carbon composite production. This transition to synthetic graphene underscores the need for further research into the role of non-crystallinity and defects in graphene for enhancing metal–graphene composites. Despite advancements in graphene production, a key challenge remains: effectively integrating defective graphene – characterized by both structural and chemical disorder – into metal grain boundaries. Our study [20] provides novel insights into metal/amorphous–graphene interfaces, advancing the understanding beyond conventional crystalline models [4,6,7].

There is a growing body of work involving computer simulations using molecular dynamics (MD) and density-functional theory (DFT) to explain atomic-level interaction in metal–graphene composites [4,6–9]. These studies describe the formation and properties of metal–graphene nanostructure but do not provide atomistically detailed information about electronic activity in the composites. Using the Kubo–Greenwood

* Corresponding author.
E-mail addresses: kn478619@ohio.edu (K. Nepal), drabold@ohio.edu (D.A. Drabold).

https://doi.org/10.1016/j.carbon.2024.119711
Received 7 August 2024; Received in revised form 23 September 2024; Accepted 14 October 2024
Available online 21 October 2024

Table 1
Structural and electronic parameters in copper–graphene composites post relaxation and DFT calculation. P = transverse component of the stress tensor. d_{Cu-G} = average interface distance between copper and graphene layer after relaxation. Φ = work-function: energy required to remove an electron from the copper surface. $\triangle q$ = net charge transfer to carbon atoms from interface copper atoms.

Cu-Gr (100)				Cu-Gr (110)				Cu-Gr (111)			
P [GPa]	d_{Cu-G} [Å]	Φ[a] [eV]	$\triangle q$ [eV/atom]	P [GPa]	d_{Cu-G} [Å]	Φ[a] [eV]	$\triangle q$ [eV/atom]	P [GPa]	d_{Cu-G} [Å]	Φ[a] [eV]	$\triangle q$ [eV/atom]
0.00[b]	3.40	3.75	0.01	0.00[b]	3.39	3.70	0.01	0.00[b]	3.20	3.50	0.02
3.00	3.03	2.85	0.01	2.71	2.97	2.68	0.01	1.50	2.67	2.49	0.05
7.50	2.70	2.15	0.03	4.53	2.51	1.93	0.03	5.60	2.36	1.00	0.08
10.5	2.52	1.89	0.03	8.50	2.40	1.52	0.04	8.40	2.32	0.95	0.09

[a] The pure copper work-functions (Φ) for (100), (110), and (111) are 4.53, 4.25, and 4.57 eV, respectively.
[b] The equilibrium configuration of the models with no vertical compression

formula (KGF) for electronic conductivity [21,22] and Space-Projected Conductivity (SPC) method [23,24], the electronic conduction activity has been spatially resolved in copper–graphene [25] and aluminum–graphene [26] systems. Identifying conductive regions can assist in the development of materials for other applications such as conducting bridge random access memory (CBRAM), physical unclonable function (PUF) devices, and other systems where atomistic insights into charge transport are essential [27–30]. Some other ways to identify conductive regions are used: the $q_i - q_j$ method based upon overlapping wavefunctions [27], and an approach based on the Kohn–Sham charge density evaluated at the Fermi level. [31].

The SPC technique has been effectively applied to analyze electronic transport paths across a variety of materials, including carbon-based systems [32,33], metals [34,35], metal–carbon composites [20,25,26], glasses [27], silicon [24], and other oxides [28,36]. While SPC provides valuable insights into transport phenomena, its computational demands can be considerable. To address this, we propose a simplified and efficient alternative to SPC, called the N^2 method, which is particularly well-suited for large systems. This approach is also easy to implement, especially in local basis DFT frameworks like the Spanish Initiative for Electronic Simulations with Thousands of Atoms (SIESTA) [37].

2. Computational methodology

2.1. Sandwich structures of copper–carbon composites

Interfacial models of copper–graphene composites were constructed as "sandwich" geometries as illustrated in Fig. 1(a), where a layer of graphene was inserted into different low-energy crystallographic orientations of copper; (100), (110), and (111). The sandwich structure maximizes interface contact, ensuring optimal interaction at the interface (properties at the interface significantly impact the overall conductivity of the system [4–7,38]). Fig. 1(b) [i–iii] depicts the atomic misalignment between carbon and copper atoms at the interface for different composites. The carbon atoms in a honeycomb lattice of graphene (lattice constant of 2.46 Å) have a lattice mismatch of ≈ 4% with (111) copper crystal (hexagonal lattice parameter of 2.56 Å). The lattice mismatch with the rectangular (110) copper lattice (lattice parameters of 2.56 Å and 3.62 Å) is ≈ 4% and ≈ 47% respectively. The interface between (100) and sp^2 carbon has the most significant lattice mismatch with ≈ 47% ((100) is a square lattice with a lattice parameter of 3.62 Å). These models were relaxed under finite compressions to form an interface. The simulated compression pushes the materials into a high-energy state with special properties and perhaps mimics the external pressure exerted on the composites during solid-phase extrusion [11–13]. It is noted that the compressed models in this work aim to represent realistic microstructures, differing from the ideal geometries typically used to study interface transport properties in composites. The vertical compression (P) on the models and their associated interfacial distances (d_{Cu-G}) are summarized in Table 1.

Geometric relaxation for the models was implemented with the conjugate gradient approach implemented within VASP [39] (Vienna *Ab initio* Simulation Package). To account for Van der Waals contributions, Grimme's D2 correction [40] was employed during the relaxation. The structural relaxation and the electronic calculations were conducted using a plane-wave basis set with a kinetic energy cutoff of 420 eV and 520 eV respectively and the self-consistent loop tolerance of 10^{-6} eV was considered for energy convergence. The projected augmented wave (PAW) potentials [41] was utilized for ion-electron interactions, and the generalized gradient approximation of Perdew–Burke–Ernzerhof (PBE) [42] was used as the exchange–correlation functional. The Brillouin zone was sampled using the Monkhorst–Pack scheme [43] with a 2 × 2 × 1 **k**-point mesh for geometrical relation and electronic conductivity calculations, while finer grids 4 × 4 × 2 **k**-point mesh was used for the density of states calculations. Periodic boundary conditions were implemented throughout that models an infinite graphene sheet sandwiched between copper matrix along the planar direction, and the graphene sheet is repeated along the transverse direction at every 20–25 Å. Electronic conductivity was calculated using the KGF, following the protocols outlined in Ref. [25].

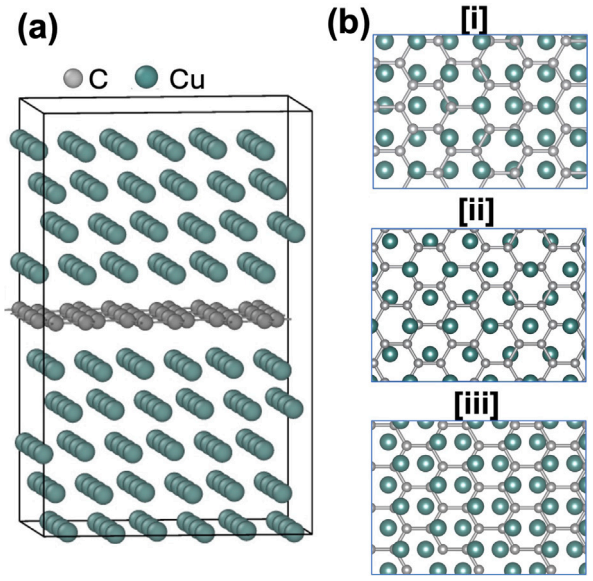

Fig. 1. (a) A typical sandwich configuration of copper–graphene interface model. (b) [i, ii, iii] depict a top view of the interface showing the arrangement of carbon atoms and copper (100), (110), and (111) grain respectively. Green and grey spheres represent copper (Cu), and carbon (C) atoms respectively. (For interpretation of the references to color in this figure legend, the reader is referred to the web version of this article.)

2.2. The N^2 method

The N^2 method is our simplified means to obtain real space information on electronic conduction. It is a consequence of the random phase approximation (RPA) implemented with the KGF [44–48]. At

low temperatures, the conductivity is determined by electrons near the Fermi energy (ϵ_f); Mott derived an equation for DC conductivity:

$$\sigma \propto [N(E)]^2\Big|_{E=\epsilon_f} \tag{1}$$

Eq. (1) indicates that the electronic conductivity, σ, is proportional to the square of the electronic density of state, $N^2(\epsilon_f)$.

Hindley arrived at the same conclusion using the RPA and Luttinger's equation for electronic conductivity [49], as detailed in [50] and briefly revisited in Appendix. Both analyses reveal that in systems with extended states near the Fermi level, conductivity scales with N^2. However, in the presence of strong disorder and localized states at ϵ_f, the assumptions underlying the RPA break down, as strong disorder can lead to Anderson localization, where wavefunctions become highly localized. For this method, the cancellation from wave-mechanical interference is assumed. For the metal–graphene system, extended states are observed near ϵ_f, making this approximation appropriate.

A question then arises; *what spatial distribution, $N^2(\epsilon_f, \mathbf{r})$, ensures that integrating this distribution provides meaningful insights into the material's conductivity?* To obtain this spatial distribution at $E = \epsilon_f$, the electronic density of states at ϵ_f is first defined as:

$$N(\epsilon_f) = \frac{1}{M}\sum_i \delta^i_f \tag{2a}$$

$$\delta^i_f = \delta(\epsilon_i - \epsilon_f) \tag{2b}$$

where i represents the band number and M is the dimension of the single-particle Hamiltonian, for example, the Kohn–Sham Hamiltonian. Brillouin zone integrals are ignored here, which is appropriate only for large cells. From Eq. (2)a, the spatial projection of $N^2(\epsilon_f)$ is obtained as:

$$\zeta(\epsilon_f, \mathbf{r}) = \frac{1}{M^2}\sum_{i,j} \delta^i_f \delta^j_f |\psi_i(\mathbf{r})|^2 |\psi_j(\mathbf{r})|^2 \tag{3}$$

Here, $|\psi_i(\mathbf{r})|^2$ is the probability density of the ith Kohn–Sham orbital at position $\mathbf{r}$. The volume integral of Eq. (3) does *not* directly yield $N^2(\epsilon_f)$, since the integral of $|\psi_i(\mathbf{r})|^2|\psi_j(\mathbf{r})|^2$ is an intricate function of the overlapping wavefunctions [27]. To fix this, modified form of Eq. (3) is taken:

$$\bar{\zeta}(\epsilon_f, \mathbf{r}) = \frac{1}{M^2}\sum_{i,j} \delta^i_f \delta^j_f |\psi_i(\mathbf{r})|^2 |\psi_j(\mathbf{r})|^2 \beta_{ij} \tag{4}$$

where β_{ij} is a correction term given as:

$$\beta_{ij} = \frac{1}{\int |\psi_i(r)|^2 |\psi_j(r)|^2 d^3r} \tag{5}$$

Next, define a non-negative density function, $\eta_{ij}(\mathbf{r})$:

$$\eta_{ij}(\mathbf{r}) = \beta_{ij} |\psi_i(\mathbf{r})|^2 |\psi_j(\mathbf{r})|^2 \tag{6}$$

By definition, $\eta_{ij}(\mathbf{r})$ vanishes for non-overlapping wave functions and modified by β_{ij}, otherwise. Eq. (4) can then be re-written as:

$$\bar{\zeta}(\epsilon_f, \mathbf{r}) = \frac{1}{M^2}\sum_{i,j} \eta_{ij}(\mathbf{r}) \delta^i_f \delta^j_f \tag{7}$$

In Eq. (7), the integral of $\bar{\zeta}(\epsilon_f, \mathbf{r})$ over the cell volume provide $N^2(\epsilon_f)$. Each grid point $\mathbf{r}$ represents a localized contribution to N^2, indicating the electronically active pathways in the material.

2.3. Interpretation of N^2 estimate for conductivity

RPA is a dramatic assumption but works well for metals and our composite — detailed in Section 3. The electronic states in such systems are extended and the phases of electronic states are averaged over the many states near the Fermi level. For localized states at the Fermi level, the RPA is expected to fail, *eg.* the off-diagonal contribution in Eq. (A.3) might be important. This work also emphasizes that the density of states at the Fermi level is not an approximate surrogate for the conductivity, whereas N^2 is.

A link to other work is noted. An effort of the early nineties was devoted to the study of localized representations of the electronic structure, either through the use of Wannier functions [51], or exploiting the decay in real space of the single-particle density matrix (DM) [52], expressed as:

$$\rho(\mathbf{r}, \mathbf{r}') = 2\sum_{i\ occ} \psi^*_i(\mathbf{r})\psi_i(\mathbf{r}') \tag{8}$$

where the sum is restricted to the occupied electronic subspace and $\mathbf{r}$ and $\mathbf{r}'$ are points in space and the system is spin unpolarized. Kohn gave a clear picture of the origin of the decay of the DM (as a function of $|\mathbf{r} - \mathbf{r}'|$) noting that it was due to quantum mechanical destructive wave interference [52]. This work was motivated partly for computational advantage, as it led to linear scaling computational demand as a function of system size, but also as basic physics of a material, since it implies a unique decay length of the DM determined by the constituent atoms and the structure of the lattice. Hindley's RPA depends on destructive wave-mechanical interference also, though the details are different than the case of ρ.

The space-projected conductivity [24] leads to an expression for σ reminiscent of the N^2 scheme and the DM. The electrical conductivity is written as a double sum on real space grid points $\mathbf{r}$ and $\mathbf{r}'$ for a Hermitian positive semi-definite matrix Γ,

$$\sigma(\omega) = \sum_{\mathbf{r},\mathbf{r}'} \Gamma(\mathbf{r}, \mathbf{r}') \tag{9a}$$

$$\Gamma(\mathbf{r}, \mathbf{r}') = \sum_{i,j} g_{ij} \left[\xi_{ij}(\mathbf{r})\right] \left[\xi_{ij}(\mathbf{r}')\right]^* \tag{9b}$$

$$\xi_{ij}(\mathbf{r}) = \psi_i(\mathbf{r})\hat{\mathbf{p}}\psi_j(\mathbf{r}) \tag{9c}$$

$$g_{ij} = \frac{2\pi e^2}{3m^2 \mathrm{V}\omega} \left[f(\epsilon_i) - f(\epsilon_j)\right] \delta\left(\epsilon_j - \epsilon_i - \hbar\omega\right) \tag{9d}$$

Here, e, m, V, ω, and f are electron charge, electron mass, the system's volume, the external Kubo field frequency, and the Fermi–Dirac distribution, respectively and $\hat{\mathbf{p}}$ is the momentum operator. Note the similarity of the expressions for Γ and ρ. Γ is built from double sum over the momentum-related objects ξ evaluated at two different points algebraically similar to the DM. However, the DM is a single sum over all the states below the Fermi level, whereas Γ is built from a small range near the Fermi energy. To the extent that there are many states in the small interval (for example in a metal), one might expect decay in $\Gamma(\mathbf{r}, \mathbf{r}')$, for large $|\mathbf{r} - \mathbf{r}'|$ which is presumably related to the validity of the RPA. By examining Δ, the diagonal part of Γ:

$$\Delta(\mathbf{r}) = \Gamma(\mathbf{r}, \mathbf{r}), \tag{10}$$

we observe that the spatial conduction activity given by Δ is usually qualitatively similar to a more intricate analysis using the full Γ.

3. Results and discussions

3.1. Copper crystallographic orientations, electronic conduction and transport

To check the proposed quadratic relationship between the full Kubo–Greenwood electronic conductivity and the density of states at the Fermi level, detailed in Section 2.2, the electronic properties of sandwich models constructed with (100), (110), and (111) copper grains are examined. An increase in electronic conductivity with compression was observed for all the configurations (see Fig. 2). The improvement in electronic conductivity in Fig. 2(a) directly correlates to the squared electronic density of states at the Fermi level, $N^2(\epsilon_f)$, in Fig. 2(b). This validates the argument that the conductivity scales as $N^2(\epsilon_f)$ and not linearly as $N(\epsilon_f)$, as intuitively defined from KGF and utilized by Watanabe et al. in Ref. [31] and in Ref. [53]. To provide

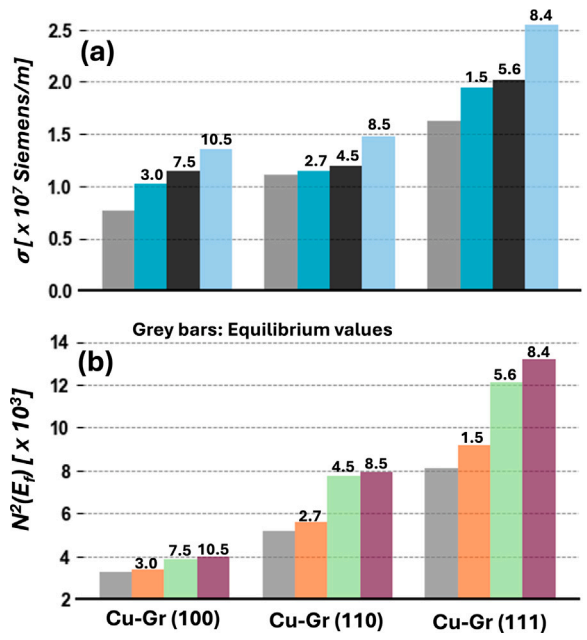

Fig. 2. Electronic Conductivity (σ) and Squared Electronic Density at Fermi level $N^2(\epsilon_f)$ in copper–graphene–copper composites. (a) Displays σ for copper grains oriented along (100), (110), and (111) at different compression values (written at the top of each bar in GPa). (b) Shows $N^2(\epsilon_f)$ for the same orientations and compressions.

additional evidence that the scaling of electronic conductivity is not linear, spatially decomposed $N(\epsilon_f)$ is presented in Section 3.1.2.

Electronic conduction in copper–graphene composites reveals a strong dependence on the crystallographic orientation of copper, with the (111) orientation exhibiting the highest conductivity, followed by (110) and then (100) grains. To study this dependence, the relaxation effects on these composites are explored. Fig. 3(a), (b), and (c) present the "top view" of the self-organized interface structures for (100), (110), and (111) copper orientations, respectively, after energy optimization, starting from the configurations shown in Fig. 1(b). While no periodic atomic alignment between carbon atoms and (100) copper atoms is observed, the interface atoms in (110) and (111) crystal orientations form near-perfect registries, creating continuous networks. These networks termed the "bridge" (110) and "top-fcc" (111) registries, see Fig. 3(b) and (c) respectively, represent low-energy, highly favorable geometries for electron transport in metal–carbon composites.

To investigate the influence of the copper–carbon interfacial configuration on the electronic transport properties of the composites, work functions (ϕ) for the composites at different compression levels are computed, summarized in Table 1. At equilibrium (no vertical compression at the copper–graphene interface), the (100) orientation exhibited the highest work function, followed by the (110) and (111) surfaces. This suggests that electrons from (111) copper are the most likely to transfer to the graphene layer. Reduced work-functions were observed in all composites as the interface distance decreased. The extent of this reduction depends on the copper orientation within the composites, as detailed in Table 1. A decreasing work-function indicates more efficient electron transfer from the copper surface to carbon atoms. This efficiency in electron transfer is quantified by computing the net charge transfer ($\triangle q$) to carbon atoms using Bader charge analysis [54]. The Bader charge for composites with varying interface distances is summarized in Table 1. A significant charge transfer of approximately 0.1 e^-/atom for the (111) interface at shorter interface distances is observed, compared to 0.04 e^-/atom and 0.03 e^-/atom for the (110) and (100) composites, respectively.

In the study by Gwalani et al., transmission electron microscopy (TEM) analysis reveals a predominant coherence of graphene flakes with the (110) copper grains and a reduced grain boundary density in copper–graphene composites compared to pure copper, contributing to the enhanced electronic conductivity. Our findings indicate that the (111) orientation forms a commensurate registry with graphene potentially dressing the grains. Additionally, the observed low-energy registry of the (110) orientation may improve the coherent alignment of copper (110) with graphene. Such coherence and commensurate registry likely facilitate enhanced electronic coupling, thereby improving global electrical conductivity.

For completeness, generalizing the reported electronic properties at elevated temperatures is not obvious and requires further investigation. Nepal et al. [26] showed that aluminum-multilayer graphene composites exhibit enhanced conductivity under compression at high temperatures, consistent with the results for solid-phase extruded composite samples [13]. This enhancement is likely due to improved interlayer contact, reduced potential barriers, and hopping between localized states driven by lattice motion at T > 0, as discussed in Refs. [55,56], and [57], as well as by Mott and Davis in Ref. [58].

3.1.1. Electronic transport from squared charge density near the fermi level

Spatially projecting N^2 involves computing the band-decomposed squared charge density as defined in Eq. (6). For this, 60 single-particle Kohn–Sham states that are within the vicinity of the Fermi level were used as wave functions. Since the electronic density of states is an intrinsic property of any quantum system, it is expected that the N^2 projections should be consistent across any complete basis set, whether constructed from plane waves, atomic orbitals, Wannier functions, or other relevant representations. The δ function in Eq. (6) was approximated with a Gaussian function with a smearing width of 0.05 eV. Although the numerical value depends on this width, the spatial projection of N^2 remained smooth and consistent.

$\bar{\zeta}(\epsilon_f, \mathbf{r})$ is shown as a heat map in Fig. 3 (d–f) for the composites with different grain orientations. The red (high intensity $\bar{\zeta}(\epsilon_f, \mathbf{r})$) depicts the region in interface with active conductive areas, while blue represents low conducive regions. A visual inspection shows that the interface between (111) copper-matrix and graphene shows higher interactive networks, followed by composites with (110) and (100) copper, depicted in Fig. 3 (d–f) respectively. These interactive regions at the contact signify graphene's role as a connecting link across the copper grains. Further, the efficiency is associated with the grain orientations.

3.1.2. Charge density near the fermi level to estimate the conduction activity in materials

Here, the density of states at the Fermi level to identify regions of active conduction activity is considered and a comparison with the results from the proposed N^2 method is offered. The electronic density of states is defined in Eq. (2)a for $E = \epsilon_f$. The spatial projection of $N(\epsilon_f)$ over the electronic states near the Fermi level is obtained as:

$$\chi(\epsilon_f, \mathbf{r}) = \frac{1}{M} \sum_i |\psi_i(\mathbf{r})|^2 \delta_f^i \tag{11}$$

As required, the volume integral of Eq. (11) results in $N(\epsilon_f)$. To compute $\chi(\epsilon_f, \mathbf{r})$, the density of states is projected onto 60 single-particle Kohn–Sham states near the Fermi level, and the δ function is approximated with a Gaussian function with a smearing width of 0.05 eV.

The spatially-resolved density of states, $\chi(\epsilon_f, \mathbf{r})$, is depicted as a heat map in Fig. 4 for composites with various grain orientations. High-intensity regions, shown in red, correspond to areas of active conduction activity at the interface, while blue regions indicate low. The heat map in Fig. 4 depicts the highest interaction between graphene and (111)-oriented copper, followed by (110) and (100) orientations. However, the conduction pathways are not as distinctly predicted by

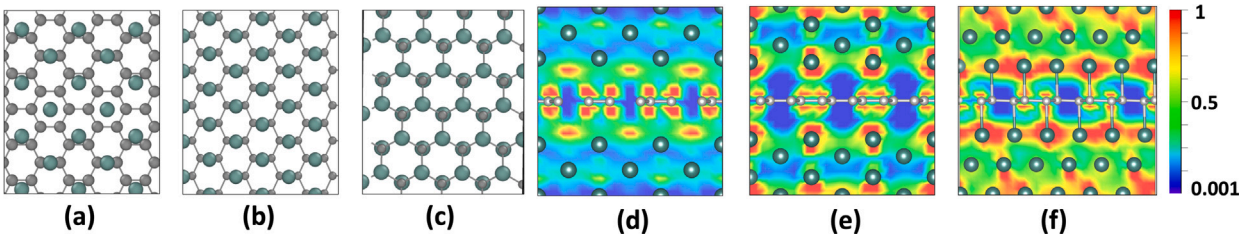

Fig. 3. (a–c) depicts the top view of composite interfaces after structural relaxation, with copper grains oriented along (100), (110), and (111) respectively. Note the remarkable metal and carbon atoms registry on the (111) orientation. The side view of these interfaces, shown in (d–f) depicts $\bar{\zeta}(\epsilon_f, \mathbf{r})$ (space projection of N^2) as a two-dimensional heat map decomposed over 60 electronic bands at the Fermi level in copper–graphene composites. Values are scaled by the maximum value in (111) copper composite. (d–f) correspond to composites with copper oriented along (100), (110), and (111) directions, respectively. The color bar represents the intensity of electronically favorable pathways, ranging from blue (low intensity) to red (high intensity). (For interpretation of the references to color in this figure legend, the reader is referred to the web version of this article.)

Table 2
Structural parameters in copper–graphene composites with different impurity concentrations. All parameters are the average values. C–N: carbon–nitrogen bond distance. δ: Shift from graphitic C–C bond length (1.42 Å). C–N–C: carbon–nitrogen–carbon bond angle. $\Delta\theta$: Shift from graphitic C–C–C bond angles (120 °). C–O: carbon–oxygen bond distance. C–S: carbon–sulfur bond distance. C–O–C: carbon–oxygen–carbon bond angle. C–S–C: carbon–sulfur–carbon bond angle N–Cu: nitrogen–copper bond distance. O–Cu: oxygen–copper bond distance. S–Cu: sulfur–copper bond distance. All distances and angles are in Å and °.

Composites	Impurities in the Graphene Layer						Impurities with Inter-facial Copper	
Cu-Gr+	C–N	δ	C–N–C	$\Delta\theta$	C–O/C–S	C–O–C/C–S–C	N–Cu	O–Cu/S–Cu
N [5%]	1.45	0.03	114.37	5.74	–	–	2.06	–
N [10%]	1.45	0.03	114.14	5.86	–	–	2.05	–
O [5%]	–	–	–	–	1.49	115.70	–	2.03
O [10%]	–	–	–	–	1.48	117.43	–	2.03
N & O [10%]	1.49	0.07	113.20	6.80	1.48	116.78	2.05	2.03
N, O, & S [15%]	1.49	0.07	113.40	6.60	1.42/1.75	110.54/105.20	1.98	2.03/2.10

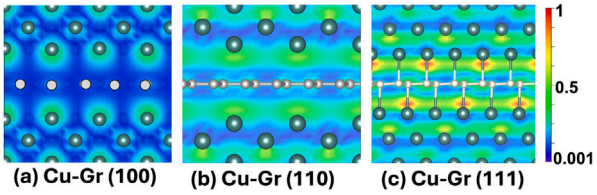

Fig. 4. The spatial projection of N, i.e., the local density of states from Kohn–Sham orbitals near the Fermi level visualized as a heatmap perpendicular to the graphene plane for composites (a) (100), (b) (110), and (c) (111) copper grains. Values are scaled by the maximum value for composite with (111) grain. The grey and green spheres are carbon and copper atoms respectively. The color bar indicates the intensity of conduction active regions increasing from blue to red. (For interpretation of the references to color in this figure legend, the reader is referred to the web version of this article.)

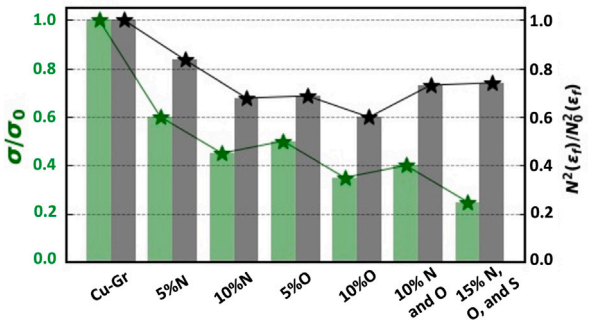

Fig. 5. [Left] Electronic conductivity (σ/σ_0) for copper–graphene composites with various impurities, where $\sigma_0 \approx 2.6\times10^7$ S/m represents the conductivity of the composite with pure graphene. [Right] Squared density of states ($N^2(\epsilon_f)/N_0^2(\epsilon_f)$) for the same systems, scaled by the value corresponding to the composite with pure graphene. The trends in $N^2(\epsilon_f)$ align closely with the changes in electronic conductivity, except for the case with sulfur due to localized states near ϵ_f.

$\chi(\epsilon_f, \mathbf{r})$. The space-resolved N distribution is more local on individual atoms, while no visible interacting network across the interface is formed. In contrast, the space projected N^2, $\bar{\zeta}(\epsilon_f, \mathbf{r})$, the patterns in images Fig. 3 (d–f) reveal more extensive and interconnected regions of high intensity, indicating the pathways that are electronically favorable.

3.2. Impurities and electronic conduction

Following the work by Ugwumadu et al. [59,60] where carbonization and graphitization of coal-like compositions were studied, it is known that nitrogen (N) tends to form a sp^2 structure with carbon (graphitic-nitrogen) while oxygen (O) and sulfur (S) form an ether bridge: C–O–C and C–S–C respectively. Based on this, interface models incorporating such carbon structures into the copper matrix are created. Specifically, models with nitrogen (5% and 10% by weight), models with oxygen (5% and 10% by weight), a model with nitrogen and oxygen (10% by weight), and a model with nitrogen, oxygen and sulfur (15% by weight) in graphene sheets are developed. These interface models are relaxed to form a low-energy configuration. Here, the interfaces with (111) copper grains are exclusively focused on.

With 5% and 10% graphitic nitrogen atoms in the sp^2 configuration, the electronic conductivities of the composites are reduced by approximately 40% and 55%, respectively, compared to composites with pure graphene ($\sigma_0 \approx 2.6 \times 10^7$ S/m). Introducing 5% and 10% oxygen at the interface reduces conductivity by ≈ 50% and 65%, respectively. Additionally, a combination of 5% nitrogen and 5% oxygen reduces the conductivity by ≈ 60%, and with 5% nitrogen, 5% oxygen, and 5% sulfur, the conductivity was reduced by ≈ 75%. This indicates that oxygen and sulfur impurities have a more detrimental effect on the overall conductivity than nitrogen impurities. Fig. 5 summarizes these observations on the left axis. Furthermore, the squared density of states was also computed and is plotted on the right axis in Fig. 5, with values scaled relative to the maximum value for the composite with pure graphene. Indeed, $N^2(\epsilon_f)$, represented by the black line in the figure, follows the trend in electronic conductivity (shown by the green line), except for the case of the model with nitrogen, oxygen, and sulfur atoms.

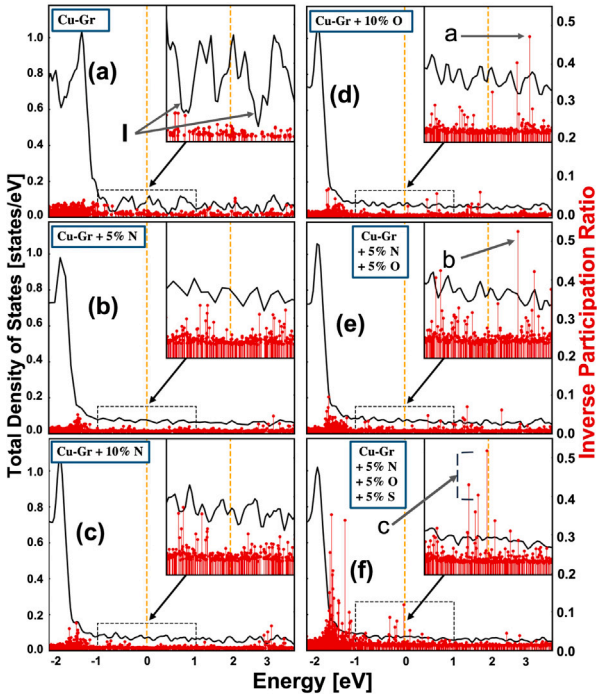

Fig. 6. Total density of states (TDoS) are shown as black plots on the left axis and inverse participation ratio (IPR) is shown by red vertical droplines on the right axis. TDoS for copper–graphene composite with (a) no impurity, (b) and (c) 5% and 10% of the nitrogen in graphene, (d) 10% of the oxygen, (e) 5% nitrogen and 5% oxygen, and (f) 5% nitrogen, 5% oxygen and 5% sulfur. The Fermi level is set at zero, shown by vertical orange lines. Insets show the high-resolution image for the energy region [-1 eV, 1 eV]. (For interpretation of the references to color in this figure legend, the reader is referred to the web version of this article.)

To analyze the significant reduction of electronic conductivity with the addition of impurities, the extent of structural disorder impurity atoms bring to the planar sp^2 structure of graphene and at the interface is examined. Table 2 provides average structural parameters and distances, illustrating the impact of impurities on graphene's structure and its interface with copper. Nitrogen impurities at concentrations of 5% and 10% lead to slight increases in the C–N bond distance, shift ≈ 0.03 Å, and deviations in the C–N–C bond angles by ≈ 5.8° from the ideal graphitic carbon, indicating significant structural disorder. Notably, with no copper surface, the graphitic nitrogen shows minimal deviation from the ideal planar structure, as reported in [59]. Incorporating oxygen and sulfur into graphene exhibited an equally or more detrimental effect. These atoms break the sp^2 coordination and migrate towards the copper atoms, forming O–Cu and S–Cu bond length at ≈ 2.03 Å and 2.10 Å. In the interface model with oxygen and nitrogen, A significant shift in C–N bond lengths (0.07 Å) and impurity-centered bond angles (shift in nitrogen-centered C–N–C is ≈ 6.80°) is observed. The presence of sulfur in the graphene sheet further deteriorates the structure. This disorder introduces the undulating graphene structure disrupting the π−conjugated graphene network at the interface (See Table 2 for detailed structural data).

Next, the electronic density of states (EDoS) for all interface models with impurities is computed. The EDoS is provided in Fig. 6(a) for copper–graphene composites with pristine graphene. The spectrum features distinct dip regions near the Fermi level (indicated by the orange vertical line), labeled "I". Additionally, the spectrum is characterized by degenerate and extended states near the Fermi level, as shown by the vertical drop lines with the small inverse participation ratio (IPR). With 5% and 10% substitutional nitrogen in the graphene interface, the reduced regions in the EDoS spectrum are filled, shown in Fig. 6(b) and (c). This is a consequence of the structural symmetry

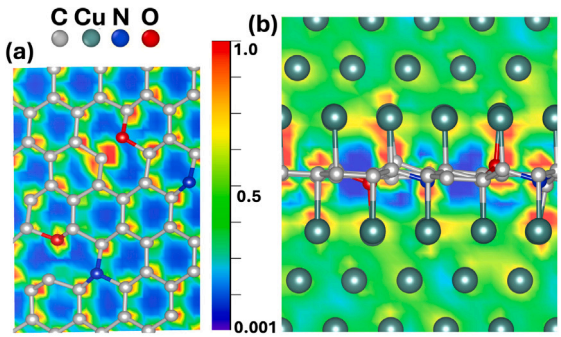

Fig. 7. The two-dimensional heat map of $\bar{\xi}(\epsilon_f, \mathbf{r})$ for copper–graphene composites with impurity atoms visualized (a) along and (b) perpendicular to the graphene plane, scaled by the maximum value. Copper, carbon, nitrogen, and, oxygen atoms are represented by green, silver, blue, and red spheres respectively. The color bar indicates the intensity of favorable conduction pathways, highlighted by regions in red or reddish-yellow. (For interpretation of the references to color in this figure legend, the reader is referred to the web version of this article.)

breaking at the interface due to impurity atoms. It is important to note that substitutional nitrogen does not contribute to localized states near the Fermi level, indicated by small IPR values. In composites containing 10% oxygen, 10% of both oxygen and nitrogen, some states with higher IPR values (labeled "a" and "b") in Fig. 6(d) and (e) are observed, indicating some degree of electronic state localization around the impurity atoms. The model with nitrogen, oxygen, and sulfur atoms introduces localized states near the Fermi level (labeled "c"), see the highlighted region in Fig. 6(f). This results in a poor agreement between KGF conductivity and N^2, demonstrated in Fig. 5. Impurity atoms result in significant structural disorders and reduced electronic conductivity, however, no strong localization of electronic states near the Fermi level was observed. To better understand how these impurities affect charge transport in graphene and the composites Bader charge of the impurity atoms and a real-space decomposition $N^2(\epsilon_f)$ is computed.

The in-plane charge density calculations reveal that impurity atoms obstruct the charge flow within the sp^2 network of graphene. They can trap carriers reducing the overall mobility of electrons in the graphene sheet, and impacting the composites' electrical conductivity. This effect is quantified by computing the Bader charge in interface models. In models with nitrogen and/or oxygen, the average Bader charge in nitrogen and oxygen was increased by ≈ 0.90 eV per atom and by 0.95 eV per atom respectively. This charge redistribution to impurity atoms reduced the average charge gained by carbon from the copper atoms. At a shorter interface distance, $d_{Cu-G} = 2.32$ Å, the average charge in carbon atoms reduced from around 0.1 eV to 0.05 eV per atom. Further, adding sulfur into these interface models with nitrogen and oxygen reduced the average charge gained by carbon atoms to 0.02 eV per atom.

Next, $\bar{\xi}(\epsilon_f, \mathbf{r})$ along the plane and transverse to the graphene layer is computed. $\bar{\xi}(\epsilon_f, \mathbf{r})$ favors pathways consisting of carbon atoms along the hexagonal structure, while impurity atoms terminate the transport, as illustrated in Fig. 7(a). Moreover, the undulating structure of graphene, coupled with impurities, disrupts the continuous network across the copper grains and hinders orbital mixing at the interface. This disruption results in reduced transport across the graphene, as evidenced by the discontinuous and weaker network of $\bar{\xi}(\epsilon_f, \mathbf{r})$, shown in Fig. 7(b), contrasting with the continuous network observed with pristine graphene at the interface (see Fig. 3(f)).

4. Conclusion

The electronic and transport properties of copper–graphene composites with different crystal orientations of copper grains and the incorporation of graphene with impurities are studied. From *ab initio*

density functional theory calculations, it was identified that the orientation of copper grains significantly influences the electronic conductivity of the composites, with the (111) orientation exhibiting the highest conductivity due to favorable contact with graphene. Our findings emphasize the importance of contact alignment in enhancing carrier transport across interfaces. This work posits that controlling the structural alignment can tailor the electronic performance of graphene-based devices, offering potential advancements in areas ranging from flexible electronics to energy storage and beyond.

A novel method, the N^2 formalism, that identifies electronically active conduction sites in materials is introduced. Using the method, visual evidence for copper–graphene composites with (111) grains demonstrating the highest electronic dynamics at the interface compared to (110) and (100) configurations is provided. Additionally, the presence of impurities, such as nitrogen, oxygen, and sulfur in graphene sheets diminishes conductivity, highlighting the sensitivity of electronic properties to defects. These results provide valuable insights into optimizing the design and fabrication of metal–graphene composites for electronic applications, emphasizing the need for precise control over structural alignment and impurity levels to harness their full potential in next-generation electronic devices.

Funding

This material is based upon work supported by the Department of Energy under Award Number DE-FE0032277. This work also used computational resources at the Pittsburgh Supercomputing Center (Bridges-2 Regular Memory) through allocation DMR190002, MAT240030, PHY230122 from the Advanced Cyberinfrastructure Coordination Ecosystem: Services & Support (ACCESS) program, funded by the U.S. National Science Foundation (NSF) grant number: 2138259, 2138286, 2138307, 2137603, and 2138296.

Disclaimer

CRediT authorship contribution statement

K. Nepal: Writing – original draft, Validation Visualization, Software, Resources, Methodology, Investigation, Formal analysis, Data curation, Conceptualization. **C. Ugwumadu:** Writing – review & editing, Visualization, Validation, Methodology, Formal analysis, Conceptualization. **F. Kraft:** Validation, Resources, Project administration, Investigation, Funding acquisition. **Y. Al-Majali:** Validation, Resources, Project administration, Investigation, Funding acquisition. **D.A. Drabold:** Writing – review & editing, Validation, Supervision, Software, Resources, Project administration, Methodology, Investigation, Funding acquisition, Formal analysis, Data curation, Conceptualization.

Declaration of competing interest

The authors declare that they have no known competing financial interests or personal relationships that could have appeared to influence the work reported in this paper.

Appendix. Random phase approximation and electrical conductivity

In the sixties and seventies, much research was on electronic eigenfunctions in disordered systems, especially near an optical gap. This was near the heart of some of the most important ideas in solid state theory at the time: Anderson localization, Mott's "mobility edge" (indeed Anderson, Mott, and Van Vleck shared the 1977 Nobel Prize in Physics for research on disordered systems). To make progress, simple approximations were invoked.

One such idea was the so-called *Random Phase Approximation* (RPA) [44–46,50], introduced to study the electrical conductivity of disordered systems. The assumption in such systems is that in conducting states the phase of the probability amplitude for finding an electron on a particular basis orbital varies randomly. Sums of such terms might be expected to exhibit considerable cancellation, and if this assumption is made, simplified (and approximate) expressions for the conductivity accrue.

Here, the RPA method of Hindley tersely is described. The method has its origins in the work of Mott [48] and Cohen [61]. It is emphasized that this is highly approximate but appears from this and other work to be useful in conjunction with visualization of conduction active parts of a complex network.

Hindley expands the energy eigenstates $\psi_i(\mathbf{r})$ as:

$$\psi_i(\mathbf{r}) = \sum_n \alpha_{i,n}\phi_n(\mathbf{r}-\mathbf{R}_n) \tag{A.1}$$

where $\phi_n(\mathbf{r}-\mathbf{R}_n) \equiv |\phi_n\rangle$ represents an orthogonal localized wave function, or more realistically, an orthonormal Wannier function,[1] centered at atomic site $\mathbf{R}_n$. The expansion coefficient is denoted as $\alpha_{i,n}$. It is noteworthy that in the present version of the argument, **k**-space dispersion has been neglected, an assumption that holds for sufficiently large systems where the entire Brillouin zone can be approximated by the Γ point, as is common in large-scale *ab initio* calculations.

From Eq. (A.1), the matrix elements for the momentum operator $\hat{\boldsymbol{p}}$ in the energy representation is:

$$P_{i,i'} = \sum_{n,n'} \alpha^*_{i',n'}\alpha_{i,n}p_{n,n'} \tag{A.2a}$$

$$p_{n,n'} = \langle\phi_n|\hat{\boldsymbol{p}}|\phi_{n'}\rangle \tag{A.2b}$$

where $p_{n,n'}$ are the momentum matrix element between the basis states.

In what follows, i and i' index energy eigenfunctions and m, m', n, n' index basis orbitals. From the Kubo–Greenwood formula, the squared momentum matrix elements are required. The average of the squared momentum matrix elements between energy eigenstates is:

$$\overline{|P_{i,i'}|^2} = \sum_{n,n'}\sum_{m,m'} \overline{\alpha^*_{i',n'}\alpha_{i',m'}\alpha_{i,n}\alpha^*_{i,m}p_{n,n'}p^*_{m;m'}} \tag{A.3}$$

The RPA *assumes* that the phases of $\alpha_{i,n}$ are "random" (more precisely of such a character that when they are summed there are cancellations so pronounced that off-diagonal terms are ignored). That is, for:

- $i \neq i'$, phase randomness averages out the off-diagonal terms.
- $i = i'$, only terms where $m = m'$ and $n = n'$ contribute significantly.

This leads to an approximate relation between the matrix elements of momentum matrix elements in the energy representation i and basis functions n:

$$\overline{|P_{i,i'}|^2} \approx \frac{1}{NV}\overline{\sum_{n,n'}|p_{n,n'}|^2} \tag{A.4}$$

[1] Realistic Wannier functions are not perfectly localized to a single site. The most localized forms decay at best as fast as the density matrix while exhibiting oscillations to preserve orthogonality [62–65].

in which N is the atomic number density and V the volume. The electronic conductivity is provided by an energy quadrature of $\kappa(E)$ near the Fermi level as [49]:

$$\kappa(E) = \frac{2\pi\hbar}{3m^2V} \sum_{i',i} |P_{i,i'}|^2 \delta(\epsilon_{i'} - E)\delta(\epsilon_i - E) \tag{A.5}$$

In this formulation, if ψ_i is an eigenstate of the Hamiltonian, then ϵ_i is the conjugate eigenvalue. The spectral function $\kappa(E)$ vanishes for energies at which states are localized. By applying Eq. (A.4), along with the definition of the density of states, $N(E)$, and making a few straightforward approximations, one finds that:

$$\kappa(E) \propto [N(E)]^2. \tag{A.6}$$

Carrying out the integral for $T \to 0$, the DC conductivity is approximately proportional to the *squared* density of states at the Fermi level:

$$\sigma \propto N^2(\epsilon_f) \tag{A.7}$$

This approximation is expected to be reasonable for extended electron states at the Fermi level, ϵ_f.

Mott carries out a similar analysis concluding that:

$$\sigma \propto \overline{|P_{i,i'}|^2}[N(\epsilon_f)]^2 \tag{A.8}$$

where, the averaged squared momentum matrix element is over electronic states at the Fermi level (such that, at $T \to 0$, $E_i = E_{i'} = \epsilon_f$). This form emphasizes that the DC conductivity is due to electronic transitions at the Fermi level.

Realistic calculations of σ require phonon scattering. This is most easily included with thermal MD simulations and by averaging the Kubo–Greenwood formula in a long simulation on the canonical ensemble [35,66,67]. Instantaneous configurations occur in which the HOMO-LUMO splitting nearly vanishes, thus enabling hopping reminiscent of a Landau–Zener process [68]. This is especially important in amorphous semiconductors where the electron–phonon coupling is large, especially near ϵ_f [69,70].

References

[1] D.M. Felicia, R. Rochiem, S.M. Laia, The effect of silver (Ag) addition to mechanical and electrical properties of copper alloy (Cu) casting product, AIP Conf. Proc. 1945 (1) (2018) 020075, http://dx.doi.org/10.1063/1.5030297.

[2] T.W. Ellis, I.E. Anderson, H.L. Downing, J.D. Verhoeven, Deformation-processed wire prepared from gas-atomized Cu-Nb alloy powders, Metall. Trans. A 24 (1) (1993) 21–26, http://dx.doi.org/10.1007/BF02669598.

[3] M.R. Akbarpour, F. Gazani, H. Mousa Mirabad, I. Khezri, A. Moeini, N. Sohrabi, H.S. Kim, Recent advances in processing, and mechanical, thermal and electrical properties of Cu-SiC metal matrix composites prepared by powder metallurgy, Prog. Mater. Sci. 140 (2023) 101191, http://dx.doi.org/10.1016/j.pmatsci.2023.101191.

[4] W. Li, D. Li, Q. Fu, C. Pan, Conductive enhancement of copper/graphene composites based on high-quality graphene, RSC Adv. 5 (98) (2015) 80428–80433, http://dx.doi.org/10.1039/C5RA15189A.

[5] F. Chen, J. Ying, Y. Wang, S. Du, Z. Liu, Q. Huang, Effects of graphene content on the microstructure and properties of copper matrix composites, Carbon 96 (2016) 836–842, http://dx.doi.org/10.1016/j.carbon.2015.10.023.

[6] M. Cao, Y. Luo, Y. Xie, Z. Tan, G. Fan, Q. Guo, Y. Su, Z. Li, D.-B. Xiong, The influence of interface structure on the electrical conductivity of graphene embedded in aluminum matrix, Adv. Mater. Interfaces 6 (3) (2019) 1900468, http://dx.doi.org/10.1002/admi.201900468.

[7] W. Wang, Y. Liu, T. Wang, K. Sheng, B. Yu, Graphene/Cu (111) interface study: The density functional theory calculations, in: 2011 International Conference on Electronics, Communications and Control, ICECC, IEEE, 2011, pp. 265–268, http://dx.doi.org/10.1109/ICECC.2011.6067884.

[8] S.D. Rad, A. Islam, A. Alnasser, Development of metal–graphene-filled hybrid composites: Characterization of mechanical, thermal, and electrical properties, J. Compos. Mater. 53 (24) (2019) 3363–3376, http://dx.doi.org/10.1177/0021998318812928.

[9] L. Adamska, Y. Lin, A.J. Ross, M. Batzill, I.I. Oleynik, Atomic and electronic structure of simple metal/graphene and complex metal/graphene/metal interfaces, Phys. Rev. B 85 (2012) 195443, http://dx.doi.org/10.1103/PhysRevB.85.195443.

[10] V.G. Konakov, O.Y. Kurapova, I.Y. Archakov, Improvement of copper–graphene composites properties due to the lubricating effect of graphene in the powder metallurgy fabrication process, Met. Mater. Int. 26 (2020) 1899–1907, http://dx.doi.org/10.1007/s12540-019-00456-3.

[11] K.S. Kappagantula, J.A. Smith, A.K. Nittala, F.F. Kraft, Macro copper-graphene composites with enhanced electrical conductivity, J. Alloys Compd. 894 (2022) 162477, http://dx.doi.org/10.1016/j.jallcom.2021.162477.

[12] B. Gwalani, X. Li, A. Nittala, W. Choi, M. Reza-E-Rabby, J. Atehortua, A. Bhattacharjee, M. Pole, J. Silverstein, M. Song, K. Kappagantula, Unprecedented electrical performance of friction-extruded copper-graphene composites, Mater. Des. 237 (2023) 112555, http://dx.doi.org/10.1016/j.matdes.2023.112555.

[13] A. Nittala, J. Smith, B. Gwalani, J. Silverstein, F. Kraft, K. Kappagantula, Simultaneously improved electrical and mechanical performance of hot-extruded bulk scale aluminum-graphene wires, Mater. Sci. Eng. B 293 (2023) 116452, http://dx.doi.org/10.1016/j.mseb.2023.116452.

[14] J. Zhang, C. Liang, J.B. Dunn, Graphite flows in the U.S.: Insights into a key ingredient of energy transition, Environ. Sci. Technol. 57 (8) (2023) http://dx.doi.org/10.1021/acs.est.2c08655.

[15] P.A. Advincula, W. Meng, L.J. Eddy, J.L. Beckham, I.R. Siqueira, D.X. Luong, W. Chen, M. Pasquali, S. Nagarajaiah, J.M. Tour, Ultra-high loading of coal-derived flash graphene additives in epoxy composites, Macromol. Mater. Eng. 308 (6) (2023) 2200640, http://dx.doi.org/10.1002/mame.202200640.

[16] A. Azenkeng, N.E. Stanislowski, J.E. Tibbetts, J.D. Laumb, Laboratory-scale coal-derived graphene process (final report), University of North Dakota Energy & Environmental Research Center, 2023, http://dx.doi.org/10.2172/1981328.

[17] Q. Zhou, Z. Zhao, Y. Zhang, B. Meng, A. Zhou, J. Qiu, Graphene sheets from graphitized anthracite coal: Preparation, decoration, and application, Energy Fuels 26 (8) (2012) 5186–5192, http://dx.doi.org/10.1021/ef300919d.

[18] S.B. Singh, N. Haskin, S.A. Dastgheib, Coal-based graphene oxide-like materials: A comprehensive review, Carbon (2023) 118447, http://dx.doi.org/10.1016/j.carbon.2023.118447.

[19] S. Zhang, Q. Liu, H. Zhang, R. Ma, K. Li, Y. Wu, B.J. Teppen, Structural order evaluation and structural evolution of coal derived natural graphite during graphitization, Carbon 157 (2020) 714–723, http://dx.doi.org/10.1016/j.carbon.2019.10.104.

[20] K. Nepal, C. Ugwumadu, A. Gautam, K. Kappagantula, D.A. Drabold, Electronic conductivity in metal-graphene composites: The role of disordered carbon structures, defects, and impurities, J. Phys. Mater. (2024) http://dx.doi.org/10.1088/2515-7639/ad261a.

[21] R. Kubo, Statistical-mechanical theory of irreversible processes. I. General theory and simple applications to magnetic and conduction problems, J. Phys. Soc. Japan 12 (6) (1957) 570–586, http://dx.doi.org/10.1143/JPSJ.12.570.

[22] D.A. Greenwood, The Boltzmann equation in the theory of electrical conduction in metals, Proc. Phys. Soc. 71 (4) (1958) 585–596, http://dx.doi.org/10.1088/0370-1328/71/4/306.

[23] K. Prasai, K.N. Subedi, K. Ferris, P. Biswas, D.A. Drabold, Spatial projection of electronic conductivity: The example of conducting bridge memory materials, Phys. Status Solidi (RRL) 12 (9) (2018) 1800238, http://dx.doi.org/10.1002/pssr.201800238.

[24] K.N. Subedi, K. Prasai, D.A. Drabold, Space-projected conductivity and spectral properties of the conduction matrix, in "form and function of disorder", Phys. Status Solidi b 258 (2020) 2000438, http://dx.doi.org/10.1002/pssb.202000438.

[25] K.N. Subedi, K. Nepal, C. Ugwumadu, K. Kappagantula, D.A. Drabold, Electronic transport in copper–graphene composites, Appl. Phys. Lett. 122 (2023) 031903, http://dx.doi.org/10.1063/5.0137086.

[26] K. Nepal, C. Ugwumadu, K.N. Subedi, K. Kappagantula, D.A. Drabold, Physical origin of enhanced electrical conduction in aluminum-graphene composites, Appl. Phys. Lett. 124 (9) (2024) 091902, http://dx.doi.org/10.1063/5.0195967.

[27] K.N. Subedi, K. Prasai, D.A. Drabold, Modeling of glasses: Electronic conduction mechanisms in $GeSe_3$: Ag and Al_2O_3: Cu, in: The World Scientific Reference of Amorphous Materials: Structure, Properties, Modeling and Main Applications Volume 1-Structure, Properties, Modeling and Applications of Amorphous Chalcogenides, World Scientific, 2021, pp. 79–105.

[28] C. Ugwumadu, K. Subedi, R. Thapa, P. Apsangi, S. Swain, M. Kozicki, D. Drabold, Structure, vibrations and electronic transport in silicon suboxides: Application to physical unclonable functions, J. Non-Cryst. Solids X 18 (2023) 100179, http://dx.doi.org/10.1016/j.nocx.2023.100179.

[29] K. Prasai, G. Chen, D.A. Drabold, Amorphous to amorphous insulator-metal transition in $GeSe_3$:Ag glasses, Phys. Rev. Mater. 1 (2017) 015603, http://dx.doi.org/10.1103/PhysRevMaterials.1.015603.

[30] D.R. Basaula, M. Daeipour, B. Feygelson, S. Nakhmanson, Predicting thermoelectric figure of merit in complex materials: What do we need to know? Acta Mater. 271 (2024) 119889, http://dx.doi.org/10.1016/j.actamat.2024.119889.

[31] B. Xiao, T. Gu, T. Tada, S. Watanabe, Conduction paths in Cu/amorphous-Ta_2O_5/Pt atomic switch: First-principles studies, J. Appl. Phys. 115 (3) (2014) http://dx.doi.org/10.1063/1.4861724.

[32] R. Thapa, C. Ugwumadu, K. Nepal, J. Trembly, D.A. Drabold, Ab initio simulation of amorphous graphite, Phys. Rev. Lett. 128 (2022) 236402, http://dx.doi.org/10.1103/PhysRevLett.128.236402.

[33] C. Ugwumadu, R. Thapa, Y. Al-Majali, J. Trembly, D.A. Drabold, Formation of amorphous carbon multi-walled nanotubes from random initial configurations, Phys. Status Solidi b 260 (3) (2023) 2200527, http://dx.doi.org/10.1002/pssb.202200527.

[34] K.N. Subedi, K. Prasai, M.N. Kozicki, D.A. Drabold, Structural origins of electronic conduction in amorphous copper-doped alumina, Phys. Rev. Mater. 3 (2019) 065605, http://dx.doi.org/10.1103/PhysRevMaterials.3.065605.

[35] K.N. Subedi, K. Kappagantula, F. Kraft, A. Nittala, D.A. Drabold, Electrical conduction processes in aluminum: Defects and phonons, Phys. Rev. B 105 (2022) 104114, http://dx.doi.org/10.1103/PhysRevB.105.104114.

[36] R. Thapa, B. Bhattarai, M.N. Kozicki, K.N. Subedi, D.A. Drabold, Structure and charge transport of amorphous Cu-doped Ta_2O_5: An ab initio study, Phys. Rev. Mater. 4 (2020) 064603, http://dx.doi.org/10.1103/PhysRevMaterials.4.064603.

[37] J.M. Soler, E. Artacho, J.D. Gale, A. García, J. Junquera, P. Ordejón, D. Sánchez-Portal, The SIESTA method for *ab initio* materials simulation, J. Phys.: Condens. Matter. 14 (11) (2002) 2745–2779, http://dx.doi.org/10.1088/0953-8984/14/11/302.

[38] C. Gong, D. Hinojos, W. Wang, N. Nijem, B. Shan, R.M. Wallace, K. Cho, Y.J. Chabal, Metal–graphene–metal sandwich contacts for enhanced interface bonding and work function control, ACS Nano 6 (6) (2012) 5381–5387, http://dx.doi.org/10.1021/nn301241p.

[39] G. Kresse, J. Hafner, Ab initio molecular dynamics for liquid metals, Phys. Rev. B 47 (1993) 558–561, http://dx.doi.org/10.1103/PhysRevB.47.558.

[40] S. Grimme, Semiempirical GGA-type density functional constructed with a long-range dispersion correction, J. Comput. Chem. 27 (15) (2006) 1787–1799, http://dx.doi.org/10.1002/jcc.20495.

[41] P.E. Blöchl, Projector augmented-wave method, Phys. Rev. B 50 (1994) 17953–17979, http://dx.doi.org/10.1103/PhysRevB.50.17953.

[42] J.P. Perdew, K. Burke, M. Ernzerhof, Generalized gradient approximation made simple [Phys. Rev. Lett. 77, 3865 (1996)], Phys. Rev. Lett. 78 (1997) 1396, http://dx.doi.org/10.1103/PhysRevLett.78.1396.

[43] H.J. Monkhorst, J.D. Pack, Special points for Brillouin-zone integrations, Phys. Rev. B 13 (12) (1976) 5188, http://dx.doi.org/10.1103/PhysRevB.13.5188.

[44] N.K. Hindley, Random phase model of amorphous semiconductors II. Hot electrons, J. Non-Cryst. Solids 5 (1) (1970) 31–40, http://dx.doi.org/10.1016/0022-3093(70)90194-8.

[45] L. Friedman, N. Mott, The Hall effect near the metal-insulator transition, J. Non-Cryst. Solids 7 (1) (1972) 103–108, http://dx.doi.org/10.1103/PhysRevB.41.12054.

[46] L. Friedman, Hall conductivity of amorphous semiconductors in the random phase model, J. Non-Cryst. Solids 6 (4) (1971) 329–341, http://dx.doi.org/10.1016/0022-3093(71)90024-X.

[47] N.F. Mott, E.A. Davis, Theory of electrons in a non-crystalline medium, in: Electronic Processes in Non-Crystalline Materials, second ed., Clarendon/Oxford University Press, Oxford, New York, 1979, pp. 11–15.

[48] N.F. Mott, Conduction in non-crystalline materials: III. Localized states in a pseudogap and near extremities of conduction and valence bands, Phil. Mag. 19 (160) (1969) 835–852, http://dx.doi.org/10.1080/14786436908216338.

[49] J.M. Luttinger, Transport theory, in: Mathematical Methods in Solid State and Superfluid Theory: Scottish Universities' Summer School, Springer US, Boston, MA, 1968, pp. 157–193, http://dx.doi.org/10.1007/978-1-4899-6435-9_4.

[50] N.K. Hindley, Random phase model of amorphous semiconductors I. Transport and optical properties, J. Non-Cryst. Solids 5 (1) (1970) 17–30, http://dx.doi.org/10.1016/0022-3093(70)90193-6.

[51] G.H. Wannier, The structure of electronic excitation levels in insulating crystals, Phys. Rev. 52 (1937) 191–197, http://dx.doi.org/10.1103/PhysRev.52.191.

[52] W. Kohn, A.D. Becke, R.G. Parr, Density functional theory of electronic structure, J. Phys. Chem. 100 (31) (1996) 12974–12980, http://dx.doi.org/10.1021/jp960669l.

[53] V.L. Deringer, N. Bernstein, G. Csányi, C. Ben Mahmoud, M. Ceriotti, M. Wilson, D.A. Drabold, S.R. Elliott, Origins of structural and electronic transitions in disordered silicon, Nature 589 (7840) (2021) 59–64, http://dx.doi.org/10.1038/s41586-020-03072-z.

[54] W. Tang, E. Sanville, G. Henkelman, A grid-based bader analysis algorithm without lattice bias, J. Phys.: Condens. Matter. 21 (8) (2009) 084204, http://dx.doi.org/10.1088/0953-8984/21/8/084204.

[55] J. Li, D.A. Drabold, Electron hopping between localized states: A simulation of the finite-temperature Anderson problem using density functional methods, Phys. Rev. B 68 (2003) 033103, http://dx.doi.org/10.1103/PhysRevB.68.033103.

[56] T.A. Abtew, D.A. Drabold, Thermally driven hopping and electron transport in amorphous materials from density functional calculations, J. Phys.: Condens. Matter. 16 (44) (2004) S5289, http://dx.doi.org/10.1088/0953-8984/16/44/025.

[57] T.A. Abtew, M. Zhang, D.A. Drabold, Ab initio estimate of temperature dependence of electrical conductivity in a model amorphous material: Hydrogenated amorphous silicon, Phys. Rev. B 76 (2007) 045212, http://dx.doi.org/10.1103/PhysRevB.76.045212.

[58] N.F. Mott, E.A. Davis, Theory of electrons in a non-crystalline medium, in: Electronic Processes in Non-Crystalline Materials, second ed., Clarendon/Oxford University Press, Oxford, New York, 1979, pp. 209–235.

[59] C. Ugwumadu, R. Olson III, N.L. Smith, K. Nepal, Y. Al-Majali, J. Trembly, D.A. Drabold, Computer simulation of carbonization and graphitization of coal, Nanotechnology 35 (9) (2023) 095703, http://dx.doi.org/10.1088/1361-6528/ad1058.

[60] C. Ugwumadu, D.A. Drabold, N.L. Smith, J. Trembly, R. Olson, E. Shereda, Y.T. Al-Majali, The structure of appalachian coal: Experiments and Ab initio modeling, Carbon 225 (2024) 119086, http://dx.doi.org/10.1016/j.carbon.2024.119086.

[61] M.H. Cohen, Electronic structure and transport in covalent amorphous semiconducting alloys, J. Non-Cryst. Solids 2 (1970) 432–443, http://dx.doi.org/10.1016/0022-3093(70)90158-4.

[62] N. Marzari, A.A. Mostofi, J.R. Yates, I. Souza, D. Vanderbilt, Maximally localized wannier functions: Theory and applications, Rev. Modern Phys. 84 (2012) 1419–1475, http://dx.doi.org/10.1103/RevModPhys.84.1419.

[63] U. Stephan, D.A. Drabold, Order-N projection method for first-principles computations of electronic quantities and wannier functions, Phys. Rev. B 57 (1998) 6391–6407, http://dx.doi.org/10.1103/PhysRevB.57.6391.

[64] U. Stephan, R.M. Martin, D.A. Drabold, Extended-range computation of wannier-like functions in amorphous semiconductors, Phys. Rev. B 62 (2000) 6885–6888, http://dx.doi.org/10.1103/PhysRevB.62.6885.

[65] P. Ordejón, D.A. Drabold, R.M. Martin, M.P. Grumbach, Linear system-size scaling methods for electronic-structure calculations, Phys. Rev. B 51 (1995) 1456–1476, http://dx.doi.org/10.1103/PhysRevB.51.1456.

[66] T.A. Abtew, M. Zhang, D.A. Drabold, Ab initio estimate of temperature dependence of electrical conductivity in a model amorphous material: Hydrogenated amorphous silicon, Phys. Rev. B 76 (2007) 045212, http://dx.doi.org/10.1103/PhysRevB.76.045212.

[67] A. Pandey, B. Cai, N. Podraza, D.A. Drabold, Electrical activity of boron and phosphorus in hydrogenated amorphous silicon, Phys. Rev. Appl. 2 (2014) 054005, http://dx.doi.org/10.1103/PhysRevApplied.2.054005.

[68] C. Zener, R.H. Fowler, Non-adiabatic crossing of energy levels, Proc. R. Soc. A 137 (833) (1932) 696–702, http://dx.doi.org/10.1098/rspa.1932.0165.

[69] D. Drabold, Anderson transition and thermal effects on electron states in amorphous silicon, J. Non-Cryst. Solids 266 (2000) 211–217, URL https://api.semanticscholar.org/CorpusID:15985502.

[70] K. Prasai, P. Biswas, D.A. Drabold, Electrons and phonons in amorphous semiconductors, Semicond. Sci. Technol. 31 (7) (2016) 073002, http://dx.doi.org/10.1088/0268-1242/31/7/073002.